Composite structure of tropopause polar cyclones

Steven M. Cavallo* & Gregory J. Hakim

University of Washington, Seattle, WA

* *Corresponding author address:* Steven Cavallo, National Center for Atmospheric Research, 3450 Mitchell Lane, Boulder, CO 80301.
E-mail: cavallo@ucar.edu

ABSTRACT

Tropopause polar vortices are coherent circulation features based on the tropopause in polar regions. They are a common feature of the Arctic, with typical radii less than 1500 km, and lifetimes that may exceed one month. The Arctic is a particularly favorable region for these features due to isolation from the horizontal wind shear associated with the midlatitude jet stream, which may destroy the vortical circulation. Intensification of cyclonic TPVs is examined here using an Ertel potential vorticity framework to test the hypothesis that there is an average tendency for diabatic effects to intensify the vortices due to enhanced upper-tropospheric radiative cooling within the vortices. Data for the analysis is derived from numerical simulations of a large sample of observed cyclones over the Canadian Arctic. Results show that there is on average a net tendency to create potential vorticity in the vortex, and hence intensify cyclones, and that the tendency is radiatively driven. While the effects of latent heating are considerable, they are smaller in magnitude, and all other diabatic processes have a negligible effect on vortex intensity.

1. Introduction

A commonly observed feature of the Arctic, tropopause polar vortices (TPVs) are extratropical, cold-core cyclones or warm-core anticyclones, can exist on monthly timescales, and can excite surface cyclones. However, little is known with regard to factors that control their intensity. These upper level disturbances are defined by closed material contours on the dynamic tropopause (a potential vorticity (PV) surface), implying that under adiabatic conditions, their fluid properties are isolated from the background environment for which

they exist. It is well understood that upper level disturbances can play a major role in extratropical cyclogenesis (e.g. Holton 1992, chap. 8-9), and that these vortices are occasionally seen as precursors to cyclogenesis in the midlatitudes when captured by the jet stream (e.g. Hakim et al. 1995; Bosart et al. 1996; Hakim et al. 1996). Although many processes may promote the intensification of TPVs, such as Rossby wave breaking, gravity wave breaking, downstream energy propagation, turbulent diffusion, and diabatic effects, wind shear is relatively weak in the high-latitude regions where TPVs are most common. This fact, combined with observations of nearly moist adiabatic lapse rates and clouds in the vicinity of vortex cores (Cavallo and Hakim 2009, hereafter CH09), are indications that diabatic effects may be essential to their maintenance and intensification. In this paper, we seek to quantify the significance of these diabatic effects, and to determine the process with the greatest impact on vortex intensity.

The motivation to understand TPVs derives in part from the observation that cyclogenesis precursors may be vortical, rather than wave-like (e.g., Hakim 2000). Such features are well identified by the PV field, and in particular, on a single potential vorticity surface that defines the "dynamic tropopause" (e.g., Morgan and Nielsen-Gammon 1998). When viewed from this perspective, upper-tropospheric disturbances can sometimes be tracked for weeks before the occurrence of surface cyclogenesis (e.g. Hakim et al. 1995; Bosart et al. 1996; Hakim et al. 1996). Observations show that these disturbances are characterized by sometimes narrow, downward intrusions of stratospheric air to much lower atmospheric levels (e.g. Uccellini et al. 1985; Davis and Emanuel 1991; Hakim 2000). Hakim (2000) analyzed a 33-year climatology of these disturbances on the tropopause, and found many were coherent vortices with radii of approximately 500-800 km, tropopause potential temperature

amplitudes of at least 8 K, and a downward intrusion of the tropopause to approximately 600 hPa. Using a 51-year climatology, Hakim and Canavan (2005) subsequently found that TPVs exhibited preferential track locations, moved equatorward on average, and could have lifetimes of over one month.

The climatology of Hakim and Canavan (2005) was extended by CH09, where it was found that TPV cyclogenesis, as well as cyclone intensification, occur in preferential locations, with the highest probability over Baffin Island in the Canadian Arctic. In addition, no significant relationship with the large-scale flow patterns was identified, and observations from radiosondes near the vortex cores suggested the importance of diabatic effects, as evidenced by the prevalence of moist adiabatic temperature profiles through the depth of the troposphere. CH09 performed a complete PV budget analysis of a single case of an intensifying cyclonic TPV and showed that radiative cooling, enhanced near the top of the cloud layer, acted to intensify the vortex while latent heating promoted weakening. The cloud-top radiative cooling effect dominated that of latent heating, leading to a net intensification of the vortex. Motivated by results for this case, the goal of the present study is to assess their generality with a hypothesis that radiative processes maintain and intensify cyclonic TPVs on average. A potential vorticity diagnostic approach is applied to numerical simulations of a large sample of cases to gather the composite diabatic tendencies associated with TPVs in a region of the Arctic where they occur most frequently.

The remainder of the paper is organized as follows. The methods used to quantify TPV intensification using a PV diagnostics approach are discussed in Section 2. A description of the numerical model and the procedure for identifying TPVs in the model data are also provided in Section 2. Verification of the model simulations is given in Section 3. Results

from a large sample of TPVs are examined and discussed in Section 4, including a component-wise examination of the diabatic PV tendencies. A summary and concluding remarks are given in Section 5.

2. Method

CH09 perform a complete budget of the Ertel potential vorticity (EPV) tendency equation (e.g. Pedlosky 1998) for a cyclonic TPV and showed that TPV intensity change could be attributed significantly to diabatic processes, while frictional effects by momentum were negligible near the tropopause. That is, defining vortex intensity here by EPV,

$$\Pi = \frac{1}{\rho}\vec{\omega_a} \cdot \nabla\theta, \tag{1}$$

then changes in TPV intensity can be reasonably well quantified when considering diabatic effects alone using the EPV tendency equation,

$$\frac{D\Pi}{Dt} \simeq \frac{\vec{\omega_a}}{\rho} \cdot \nabla\frac{D\theta}{Dt}, \tag{2}$$

where ρ is the density, $\omega_a = \vec{\omega} + 2\vec{\Omega} = \nabla \times \vec{U} + 2\vec{\Omega}$ is the absolute vorticity, $\vec{U} = (u, v, w)$ is the three-dimensional velocity vector, and $\vec{\Omega}$ is Earth's rotational vector. The time rate of change following the fluid is given as

$$\frac{D}{Dt} = \frac{\partial}{\partial t} + u\frac{\partial}{\partial x} + v\frac{\partial}{\partial y} + w\frac{\partial}{\partial z},$$

the gradient operator is

$$\nabla = \left(\frac{\partial}{\partial x}, \frac{\partial}{\partial y}, \frac{\partial}{\partial z} \right),$$

and potential temperature is

$$\theta = T \left(\frac{p_o}{p} \right)^{R/c_p}$$

where T is temperature, p is pressure, $p_o = 10^5$ Pa is a standard constant, $R = 287$ J K^{-1} kg^{-1} is the dry air gas constant, and $c_p = 1004$ J K^{-1} kg^{-1} is the specific heat capacity of dry air at constant pressure. Note that in the subsequent analysis, the above equations are transformed to isobaric coordinates, where the hydrostatic approximation is then applied to compute ω_a and Π.

In this study, we use a numerical model described below to quantify the composite EPV tendencies of cyclonic TPVs using an isobaric version of (2). Diabatic tendencies are computed using the model's thermodynamic energy equation, which takes the following form:

$$\frac{D\theta}{Dt} = \dot{\theta}_{rad} + \dot{\theta}_{lh} + \dot{\theta}_{pbl} + \dot{\theta}_{cumulus} + \dot{\theta}_{mix}, \tag{3}$$

where $\dot{\theta}_{rad}$, $\dot{\theta}_{lh}$, $\dot{\theta}_{pbl}$, $\dot{\theta}_{cumulus}$ and $\dot{\theta}_{mix}$ are the diabatic tendencies due to parameterizations of radiation, latent heating, planetary boundary layer processes (i.e., sensible and latent heat fluxes, local and nonlocal boundary layer mixing, and entrainment), convection, and dissipation, respectively. The tendency terms of the right-hand side of (3) are then used to calculate the EPV tendencies given by (2). CH09 used this method in a case study of a particularly long-lived, large amplitude, cyclonic TPV. It was found that the radiation term in (3) contributed most significantly to vortex intensification, and although latent heating

acted to weaken the vortex, the net effect of latent heating was smaller than radiation. The goal of this study is to examine whether the results of this case study apply in general to a much larger sample of TPVs.

a. Model setup

The composite structure of cyclonic TPVs is evaluated during the time period from 2 August 2007 to 31 July 2009 for a limited-area domain over a region of the Arctic where the climatological frequency of cyclonic TPVs is high. We use the Advanced Research Weather (ARW) version of the Weather Research and Forecasting (WRF) model version 2.2.1 (Skamarock et al. 2005) and the WRF Pre-Processing System (WPS) Version 2.2. Time integration is achieved by a 3rd-order accurate Runge-Kutta method, and horizontal advection by a 5th-order accurate scheme. A horizontal grid spacing of $\Delta x = \Delta y = 30$ km is used, with 31 vertical levels and a model time step of $\Delta t = 120$ seconds. The following physics schemes are used: Rapid Radiative Transfer Model (RRTM) longwave radiation (Mlawer et al. 1997), the National Aeronautics and Space Administration (NASA) Goddard shortwave radiation (Chou and Suarez 1994), WRF single-moment (WSM) 5-class microphysics (Hong et al. 2004), Kain-Fritsch cumulus convection (Kain and Fritsch 1993), Yonsei University (YSU) planetary boundary layer (Hong and Pan 1996), thermal diffusion surface physics (Chen and Dudhia 2001a; Chen and Dudhia 2001b), and Monin-Obukhov surface layer physics (Paulson 1970; Dyer and Hicks 1970; Webb 1970). Forecasts are initialized using Global Forecasting System (GFS) analyses at 00 UTC daily, with boundary conditions derived from GFS forecasts every 3 h. The simulations are performed on a polar stereographic map projection, with a center latitude and longitude of 68.46°N and 81.14°W

with 120 x and y grid points respectively.

The model domain is shown in Fig. 1, which corresponds to a region in the Canadian Arctic. Regions of high density for cyclonic TPV intensity change have previously been determined by CH09 using 2.5° National Centers for Environmental Prediction–National Center for Atmospheric Research (NCEP–NCAR) reanalysis data every 6 h during 1948-1999 (Kalnay and collaborators 1996). The data show that the densest region is found near northern Baffin Island in the Canadian Arctic. In order to maximize the cyclone sample potential, a domain was chosen to surround this most likely climatological region. Another advantage of this particular domain is the presence a relatively dense radiosonde network, which provide an additional observation source in the model analyses used for verification. The model simulations were performed in real time during the two-year period.

b. Vortex identification

Cyclonic vortices are objectively identified using the following procedure. First, the minimum potential temperature on the dynamic tropopause, defined as the 2 PVU (1 PVU is 1×10^{-6} K kg^{-1} s^{-1} m^2) surface, is determined at the analysis time. If the minimum value is at least two standard deviations below the domain mean, then the data is further considered as a possible vortex to be include in the composite sample. This threshold is intended to retain only those cyclones with minimum tropopause potential temperature values significantly lower than the background; however, if the variance about the domain-mean value is small, the vortex amplitude does not need to be large to meet this condition. A vortex is included in the composite sample if it lies entirely within the bounds of the

domain. This condition is satisfied if a sign reversal in the gradient of potential temperature can be found in each direction along eight equally spaced radials. The minimum tropopause potential temperature value along the eight radials at the location of the sign reversal is defined as the last closed contour, and vortex amplitude is defined as the absolute difference between the last closed contour and the core value. Composite maps are created by averaging all fields relative to the grid point corresponding to the vortex core. No data within five grid points of the domain boundaries are used at any time and are not included in the composite sample. Since the fields are averaged relative to the vortex core on a fixed domain, the distance of the vortices from the domain edge is different for each sample, and the number of samples is greatest within the vortex and decreases radially outward. Due to the limited geographical area covered by the domain, it is not possible to objectively track cyclonic TPVs through their entire lifespan. Although vortices can be tracked within the domain, we choose instead to focus on their composite structure with attention given to the mechanisms of intensity change. Therefore, the number of vortex samples does not correspond to the number of individual vortex tracks, and simply represents a count of the vortex samples using the criteria above. With these criteria, a total of 568 vortex samples have been obtained during the period 2 August 2007-31 July 2009, out of 683 total model simulations.

An unfiltered set of vortices is used as a comparison to the procedure described above. In the unfiltered data, vortices are identified using the same criteria described above, except that no amplitude threshold is applied to tropopause potential temperature minima, and all vortices present in the domain at the analysis time are included. The effect of the vortex identification procedure is quantified in Fig. 2, which provides a comparison of the probability density functions (PDFs) of vortex radii and amplitude for the composite sample

and the unfiltered sample. Note that without filtering, multiple vortices can be found at any analysis time, whereas only one vortex can be found using the filtering criteria defined above. Cyclones have an average radius of 465 km, while the unfiltered cyclones have an average radius of 358 km taken from 1997 samples (Fig. 2a). Radii from both samples are generally less than 1000 km with the peak in the distribution occurring near the mean. Small cyclones are preferentially eliminated by the filter, with the peak reduction at a radius of 275 km. The average cyclone amplitude is 20.7 K in the composite data and 14.3 K in the unfiltered sample (Fig. 2b). These results indicate that filtering eliminates mainly smaller-amplitude, smaller-scale vortices, with the greatest reduction in vortices with amplitudes around 8 K. In both samples, a rather long tail is present in the amplitude distribution, with cyclone amplitudes reaching 50 K. To ensure consistency with reality, results for verification of the model simulations against GFS analyses is provided in the following section.

3. Tropopause polar cyclone verification

The WRF model forecasts are verified against GFS analyses. The GFS model has a native horizontal resolution of T382 which is re-gridded to a latitude–longitude grid with a resolution of 1° in the data available for this study. Of greatest importance here is the model bias, B, which, for a particular field at grid point j, is defined here as the average error of the WRF model forecast relative to GFS analysis,

$$B_j = \frac{1}{N} \sum_{i=1}^{N} (W_{i,j} - G_{i,j}) \,, \tag{4}$$

where N is the sample size, $W_{i,j}$ is the WRF forecast field of sample i at grid point j, and $G_{i,j}$ is the GFS analysis field of sample i at grid point j. GFS fields are interpolated to the WRF grid so that the calculation above is performed on one numerical grid; biases will also be considered relative to the vortex core. A complementary alternative to the grid-based bias definition used here is observation-based bias. Since observations of the vortex core are infrequent, the grid-based approach is chosen; the two approaches are related through data assimilation, which consistently spreads information from observations across the GFS grid.

WRF tropopause potential temperature forecast biases are shown in Fig. 3. Biases in both the 24- and 48-hour WRF forecasts are generally less than 1.5 K in magnitude and there is no clear sign preference in the domain. Biases are higher in localized areas, and appear to be largest in magnitude near radiosonde stations. This result probably reflects the assimilation process, since the GFS analyses are based upon a weighting of observations and a six-hour forecast (Derber et al. 1991), whereas no observation adjustments are made in the WRF forecasts. For 48-hour forecasts, the bias pattern is roughly similar to, but larger magnitude than the 24-hour forecasts. The largest biases are present near Cambridge Bay, Nunavut, The Pas, Manitoba, and Aasiaat, Greenland. Given that both tropopause potential temperature and EPV are highly derived quantities, we conclude that WRF forecasts are reasonably consistent, on average, with the GFS analyses.

Next we consider vortex-relative bias, where fields are averaged relative to the vortex core. Sample frequency decreases away from the vortex core so that there is less confidence in the bias near the domain edges. At the vortex core on the tropopause, 24 h forecasts of WRF potential temperature are nearly 1 K lower than GFS analyses, while biases decrease radially outward, indicating a slightly stronger vortex in the WRF forecasts than is analyzed,

on average (Fig. 4a). Away from the vortex, WRF forecasts have a positive bias at nearly all levels, with the smallest biases near the tropopause. WRF 24 h water vapor mixing ratio is biased to smaller values to the east of the vortex core, and along the tropopause (Fig. 4b). Bias in 500 hPa geopotential height (Fig. 4c) reflects lower 500 hPa heights in the 24h WRF forecasts, and a southeastward displacement of the location of the 500 hPa height minimum compared to GFS analyses. A similar pattern is apparent in tropopause potential temperature, with values southeast of the vortex core ∼2 K lower in WRF 24-hour forecasts, again reflecting displacement of the vortex core (Fig. 4d). The biases observed here are potentially attributable to some extent to different horizontal grid resolution. The WRF grid is evenly spaced with 30 km horizontal resolution, whereas the GFS grid spacing is 111 km × ∼40 km in the zonal and meridional directions, respectively, at the center of the domain. In any event, the bias is sufficiently small to proceed with a diagnostic analysis. We begin the analysis by examining the composite structure of cyclonic TPVs using WRF.

4. Composite structure

Tropopause polar cyclone density during the 2-year period is greatest along the northwestern tip of Baffin Island, Canada, as well as in the northern portions of Ellesmere Island, Canada, and northern Greenland (Fig. 5). Other areas of relatively large density include northern Baffin Bay and the northern Canadian Archipelago region. The region of large cyclone density over northern Baffin Island is located near the region of maximum cyclone intensification (cf. Fig. 1) and event density (Hakim and Canavan 2005) found in the NCEP–NCAR Reanalysis climatology.

In order to compare the composite vortex data to the background environment, uncondi-

tional composites are also performed along a fixed cross section, oriented from west to east near the center of the domain, in close proximity to radiosonde stations near Fort Smith, Baker Lake, Coral Harbour, and Iqaluit (see Fig. 3). The fixed cross section is referred to here as the background cross section, and anomalies are defined as the difference between the vortex-relative composite and the background composite (vortex composite − background composite). Although vortices may be sampled as part of the background, we expect their distribution is random, having a minor effect on the background; results shown subsequently confirm this expectation. A fixed point near the center of the cross section, near the Coral Harbour radiosonde station, is chosen to represent a background sounding for comparison with profiles in the vortex core. For the vortex-core composite, the tropopause is located near ∼600 hPa, which compares with ∼350 hPa in the background (Fig. 6a). Temperature anomalies with respect to the background sounding are negative in the troposphere and positive in the stratosphere above ∼375 hPa, with the greatest anomalies located around 700 hPa and 250 hPa, respectively (Fig. 6b). Relative humidity anomalies follow roughly the same pattern as temperature but are of opposite sign, with the greatest anomalies located around 800 hPa and 375 hPa in the troposphere and stratosphere, respectively. A positive EPV anomaly is found at nearly all levels, with a peak near 300 hPa.

Seasonal variations are evident in the vortex core profiles (Fig. 7). In Winter and Spring, tropospheric lapse rates are relatively small, with a poorly distinguished tropopause near 600 hPa (Fig. 7a,b). Moreover, only a relatively subtle temperature and dewpoint transition exists across the tropopause during Winter and Spring. Tropospheric lapse rates are larger in Summer, with an average in the vortex of ∼7.4 K km^{-1}, with large relative humidity, especially in the lower troposphere (Fig. 7c). The tropopause is well defined in summer,

locate near 500 hPa. In Autumn, the tropopause lowers to ∼575 hPa, and tropospheric lapse rates decrease to ∼6.6 K km^{-1} (Fig. 7d). In all seasons, the difference in tropopause pressure between the vortex core and background environment varies little from ∼200-250 hPa, with a slightly larger value in the autumn.

Regarding the horizontal structure of the composite vortex, Fig. 8a shows that the tropopause potential temperature is 280 K in the vortex core averaged over all seasons. The larger gradient south of the vortex core results from the background meridional potential temperature gradient, with warmer potential temperature in the southern portion of the domain on average. 500 hPa geopotential height exhibits a similar pattern, with the lowest height in the vortex core, 5110 meters, and the highest height, ∼5350 meters, located roughly 1500 km southwest of the vortex core of (Fig. 8b).

Vertical east–west cross sections through the composite vortex reveal cold (warm) temperature anomalies of −8.5 K (+5.5 K) relative to the background are centered on the vortex under (above) the tropopause (Fig. 9a). Anomalous winds are cyclonic around the vortex core, with maximum speeds of about 14 m s^{-1} 400 km from the vortex core near the steepest slope in the tropopause (Fig. 9b). A positive EPV anomaly is located above the composite tropopause, with the greatest anomalies of ∼4 PVU near the background tropopause (Fig. 9c). A downward intrusion of relatively drier, stratospheric, air is evident as a negative relative humidity anomalies of over 25% centered near the background tropopause in the vortex core (Fig. 9d). In contrast, relative humidity is anomalously high under the vortex tropopause, and slopes upward and eastward relative to the vortex. This pattern of anomalously high (low) relative humidity under (over) the vortex core creates an anomalously steep relative humidity gradient across the tropopause, which is important for the radiative

creation of EPV as will be shown below.

Composite west–east cross sections of the potential temperature diabatic tendency terms on the right-hand side of (3) are shown in Fig. 10. Total diabatic heating rates are negative, except in the lowermost troposphere near the region with anomalously high relative humidity (Fig. 10a). The largest cooling rates are found along the tropopause, particularly inside and to the east of the vortex. This pattern results in anomalous diabatic cooling (heating) centered on the vortex (background) tropopause (Fig. 10b). Radiative cooling rates are less than -0.6 K day^{-1} at all locations, with the largest cooling rate of -2 K day^{-1} on the tropopause in the vortex core (Fig. 10c). The anomalous radiative heating rate pattern is similar to the anomalous total diabatic heating rate pattern, with cooling (heating) centered on the vortex (background) tropopause (Fig. 10d). Latent heating rates are positive above $\sim$925 hPa and greatest east of the vortex core, reaching around $+2$ K day^{-1} (Fig. 10e). Below this level, latent cooling is consistent with sublimation or evaporation below a precipitating cloud layer, which are frequently observed in the Arctic throughout the year (e.g. Curry et al. 1996; Walsh et al. 2009). Anomalously large latent heating rates are present inside and to the east of the vortex core (Fig. 10f) in the region of anomalously large relative humidity.

The anomalous latent heating pattern suggests an asymmetry in the vertical motion field relative to the vortex core. Indeed, results show ascent is greatest $\sim$400 km east of the vortex core near 600 hPa, and an additional region of ascent $\sim$800 km east of the vortex core (Figs. 11). A region of relatively weaker descent is centered $\sim$300 km west of the vortex core near the tropopause, extending across the vortex core. We hypothesize that this vertical motion pattern is forced both radiatively and by the mean background shear across

the vortex. Specifically, the gradient in radiative heating (see Fig. 10d) is expected to force a nearly symmetric circulation with subsidence in the vortex core surrounded by ascent on the vortex peripheries (e.g. Eliassen 1951; Zierl and Wirth 1997), whereas the presence of mean shear across the vortex is expected to produce a dipole of vertical motion across the vortex with rising motion located downshear of the vortex core. To qualitatively assess the relative size of these contributions, the vertical motion is separated into components symmetric and asymmetric relative to the vortex core (Figs. 11b,c). The asymmetric portion dominates, and appears to be qualitatively in accord with expectations based on geostrophic vorticity advection by the thermal wind (e.g. Bluestein 1992 eqn. 5.7.42), with rising (sinking) air in regions of positive (negative) geostrophic vorticity advection by the thermal wind east (west) of the vortex core (Fig. 11d).

The corresponding composite EPV anomaly cross sections from the right-hand side of (2) are shown in Fig. 12. Anomalous EPV generation of 0.28 PVU day^{-1} at 450 hPa is located $\sim$100 hPa above the vortex tropopause (Fig. 12a). Anomalous EPV generation extends downward below the tropopause to nearly 600 hPa and upward to $\sim$350 hPa. A similar pattern is present in the anomalous EPV tendency from the radiative diabatic component, except with slightly larger magnitude for EPV generation in the vortex compared to the full diabatic term (Fig. 12b). EPV destruction from latent heating extends from $\sim$750 hPa upward to 400 hPa (Fig. 12c). EPV tendencies from all other diabatic components are small in comparison to the full diabatic term (Fig. 12d).

These results show that, for a large sample of TPVs in the Canadian Arctic, cyclonic EPV generation is present in the vortex, and therefore there is a tendency for TPVs to intensify on average due to radiative processes. The anomalous EPV tendency pattern

may be understood by appealing to the vertical vorticity component term in (2), so that $\frac{D\Pi}{Dt} \simeq \frac{\zeta_a}{\rho}\frac{\partial \dot{\theta}}{\partial z}$. Comparison of Figs. 12a,b to Figs. 10b,d suggest that the EPV generation is largely established by the enhanced vertical heating gradient from anomalous radiative cooling (heating) at the vortex (background) tropopause. As there is also a qualitatively similar relative humidity pattern with an enhanced vertical relative humidity gradient near the tropopause (cf. Fig. 9d), we hypothesize that changes in the vertical moisture distribution play an important role in creating the radiative anomalies that result in the vortex intensification seen here. The specific role that changes in vertical moisture gradients may have on vortex intensity change is beyond the scope of the present study, and will be explored in a future study.

a. Seasonal variability

While it is well known that Arctic temperature and radiative fluxes have large seasonal variations (e.g. Peixoto and Oort 1992 Ch. 6; Serreze et al. 2007), it is unclear if or how these variations affect TPV intensification. For example, with seasonal temperature variations of over 50 K in some regions of the Arctic (e.g. Peixoto and Oort 1992 Ch. 7), large variations in latent heating might be expected due to the exponential relationship between temperature and saturation vapor pressure. Here we briefly examine the seasonal dependence of TPV structure and intensity tendency for the two-year period of interest.

Comparing seasonal composite tropopause potential temperature anomalies reveals that they are largest during the winter and spring, with anomalies of -25 K and -27 K respectively (Fig. 13a,b), compared to -21 K and -22 K in summer and autumn, respectively (Fig. 13c,d). This result is similar to those of Hakim and Canavan (2005), where it was found that

cyclone amplitude is smallest in summer. The horizontal scale of the composite vortex anomalies varies little, but is smallest in winter and autumn (Fig. 13a-d). Comparing vertical cross sections by season indicates that the magnitude of the temperature anomalies is considerably larger in summer, particularly in the lower stratosphere, with anomalies of +6.5 K compared to +2.5 K in Winter (Fig. 14a,b). We hypothesize that this additional warming is due to the absorption of solar radiation by ozone, which is absent in the winter. Relative humidity anomalies exhibit a pattern similar to temperature, with much larger anomalies in the summer (Fig. 14c,d). In contrast, radiative heating anomalies above the tropopause are of nearly the same magnitude in both the winter and summer, except the vertical extent is larger in the summer. Moreover, stratospheric warming is found on larger horizontal scales than the vortex anomalies, which again is potentially due to ozone. Radiative cooling is considerably stronger near the vortex tropopause in summer (Fig. 14e,f), with the anomalies shifted upward by ∼100 hPa relative to winter. This shift appears to be co-located with the area of anomalously large vertical gradient of relative humidity near the vortex core (cf. Fig. 14c,d).

The upward shift in the radiative heating anomalies is important because it implies an upward shift in the region of EPV generation into the lower stratosphere in summer. Results largely confirm this expectation, with smaller EPV tendencies, by a factor of ∼1.5, in winter, except for slightly larger values on the tropopause inside the vortex (cf. Fig. 15a,b). A similar pattern is found for the EPV tendency due to radiation (cf. Figs. 15c,d) , with the EPV tendency smaller by a factor of ∼2.15 in winter. The magnitude of the EPV tendency from the latent heating component also exhibits a strong seasonal difference, with maximum EPV destruction on the tropopause smaller by a factor of ∼2.6 in winter (cf. Fig. 15e,f).

These seasonal differences are consistent with those due to warmer clouds of greater optical thickness, with higher latent heating rates inside the cloud, and stronger cloud-radiative effects in regions of increased hydrometeor gradients as would be expected in summer. These results suggest that an interesting sensitivity may exist in the relationship between radiative and latent heating processes. With globally averaged surface temperatures predicted to continue to increase over the next century (IPCC 2007), and Arctic temperature increases expected to be greater than the global average due at least in part to an ice-albedo positive feedback (e.g. Cess et al. 1991), further examination of this sensitivity is of particular interest for future work.

5. Summary and conclusions

A previous case study showed that TPV intensification was due to radiative processes (Cavallo and Hakim 2009), which motivated the hypothesis explored here that cyclonic TPV maintenance and intensification is radiatively driven. Diabatic mechanisms that affect cyclonic tropopause polar vortex (TPV) intensity were quantified using a mesoscale numerical model and a potential vorticity framework on a large sample of cases. The geographical region of interest was chosen based on previous studies that identified regions of largest TPV density (Hakim and Canavan 2005) and intensification (Cavallo and Hakim 2009) near Baffin Island in the Canadian Arctic. Objective criteria were used to identify vortices in the model gridded data, yielding a sample of 568 events.

The composite results support the hypothesis, showing that there is an average tendency for TPVs to diabatically intensify, and that radiation is the dominant component of intensi-

fication. While latent heating had a significant affect on vortex intensity by destroying EPV near the tropopause, the magnitude was smaller than radiation by a factor of approximately 1.5; all other diabatic tendencies were small in comparison. Moreover, seasonal composite EPV tendencies showed that radiation intensifies vortices on average during both the summer and winter, which differ substantially in that solar radiation is absent (nearly continuous) in winter (summer). Furthermore, while EPV destruction due to latent heating increases in the summer, radiative EPV creation also increases. However, the radiatively generated region of EPV in the vortex shifts slightly upward, away from the tropopause in the summer, and therefore no additional intensification is apparent at that level. Composite diabatic tendencies further revealed that the radiative EPV creation in the vortex core is associated with an enhanced vertical radiative heating gradient across the vortex tropopause. This enhanced gradient arises from anomalously large radiative cooling centered just under the vortex tropopause, and anomalously small radiative cooling in the lower stratosphere near the level of the background tropopause. The radiative cooling pattern in the vortex is qualitatively similar to the composite relative humidity anomalies.

The vertical distribution of the background longwave radiative cooling rates found here agree reasonably well with those predicted by Manabe and Strickler (1964), and the particular longwave radiation scheme used to obtain the results here has been validated with line-by-line calculations (Mlawer et al. 1997), which have also been validated with observations (Clough and Iacono 1995). With regard to latent heating, the resulting EPV tendencies exhibit the same patterns of EPV destruction (creation) in lower (upper) atmospheric levels seen in midlatitude storm systems (e.g. Davis and Emanuel 1991; Davis 1992; Stoelinga 1996; Lackmann 2002). Although the magnitude of the latent heating rates are considerably

smaller here, they are qualitatively consistent with expectations given the colder Arctic temperatures. Low-level latent heating patterns suggest frequently occurring clouds, which is consistent with observations from radar and lidar, which show a high frequency of cloud cover in the Arctic, with an annual cloud cover frequency of 85%, and a cloud base most frequently 0.25-1.0 km above the ground (Intrieri et al. 2002).

In terms of vortex structure, the Arctic tropopause cyclones studied here have similar characteristics to a 33-year composite of coherent tropopause disturbances in the Northern Hemisphere presented in Hakim (2000). While cyclonic TPVs exhibit slightly smaller radii scales in the present study, with mean radii of 465 km compared to 500–800 km, many characteristics are similar, most notably a lowered tropopause to ∼550 hPa, and tropopause potential temperature anomalies around 20 K. Vertical motion exhibits an asymmetric dipole pattern across with vortex, with rising air downshear and sinking air upshear of the vortex. Sinking air overlaps the vortex core, consistent with enhancement of vorticity near the tropopause by vortex stretching. We attribute the dipole pattern to a balanced circulation due to the vertical shear near the vortex associated with the average meridional temperature gradient, and sinking air in the vortex to a balanced circulation in response to radiative cooling near the vortex tropopause.

Results here suggest a possible connection between vortex intensification and radiative processes associated with moisture anomalies, especially with anomalously dry stratospheric air and moist tropospheric air. Latent heating, which adversely affects vortex intensity, is limited by the cold temperatures of the Arctic, and this may be a factor that inhibits the intensification of cold-core vortices in warmer background environments. Future research will be devoted to idealized experiments designed to explore these relationships. Finally, as

the Arctic warms and sea ice declines (e.g. Comiso et al. 2008), the relative importance of latent heating may increase, and thus could have an effect on vortex intensification. This is also a natural topic for future study.

Acknowledgments.

This work was performed as a portion of the author's Ph.D. dissertation at the University of Washington. The authors thank Profs. Dale Durran, Qiang Fu, and Mike Wallace for their thoughtful discussions and comments regarding this work. This research was sponsored by the National Science Foundation through award ATM-0552004 made to the University of Washington.

REFERENCES

Bluestein, H. B., 1992: *Synoptic-Dynamic Meteorology in Midlatitudes Volume I: Principles of Kinematics and Dynamics*, Vol. 1. Oxford University Press, 431 pp.

Bosart, L. F., G. J. Hakim, K. R. Tyle, M. A. Bedrick, W. E. Bracken, J. J. Dickinson, and D. M. Schultz, 1996: Large-scale antecedent conditions associated with the 12-14 March 1993 cyclone ("Superstorm '93") over eastern North America. *Mon. Wea. Rev.*, **124**, 1865–1891.

Cavallo, S. M. and G. J. Hakim, 2009: Potential vorticity diagnosis of a tropopause polar cyclone. *Mon. Wea. Rev.*, **137 (4)**, 1358–1371.

Cess, R. D., et al., 1991: Interpretation of snow-climate feedback as produced by 17 general-circulation models. *Science*, **253 (5022)**, 888–892.

Chen, F. and J. Dudhia, 2001a: Coupling and advanced land surface-hydrology model with the Penn State-NCAR MM5 Modeling System. Part I: Model implementation and sensitivity. *Mon. Wea. Rev.*, **129 (4)**, 569–585.

Chen, F. and J. Dudhia, 2001b: Coupling and advanced land surface-hydrology model with the Penn State-NCAR MM5 Modeling System. Part I: Preliminary model validation. *Mon. Wea. Rev.*, **129 (4)**, 587–604.

Chou, M. .-D. and M. J. Suarez, 1994: An efficient thermal infrared radiation

parameterization for use in general circulation models. NASA Tech. Memo. 104606, 3. 85 pp.

Clough, S. A. and M. J. Iacono, 1995: Line-by-line calculation of atmopsheric fluxes and cooling rates 2. application to carbon dioxide, ozone, methane, nitrous oxide, and the halocarbons. *J. Geophys. Res.*, **16 (D8)**, 519–16,535.

Comiso, J. C., C. L. Parkinson, R. Gersten, and L. Stock, 2008: Accelerated decline in the Arctic sea ice cover. *Geophys. Res. Lett.*, **35**, L01 703.

Curry, J. A., W. B. Rossow, D. Randall, and J. L. Schramm, 1996: Overview of Arctic cloud and radiation characteristics. *J. Climate*, **9**, 1731–1764.

Davis, C. A., 1992: A potential-vorticity diagnosis of the importance of initial structure and condensational heating in observed extratropical cyclogenesis. *Mon. Wea. Rev.*, **120 (11)**, 2409–2428.

Davis, C. A. and K. A. Emanuel, 1991: Potential vorticity diagnostics of cyclogenesis. *Mon. Wea. Rev.*, **119 (8)**, 1929–1953.

Derber, J. C., D. F. Parrish, and S. J. Lord, 1991: The new global operational analysis system at the National Meteorological Center. *Wea. Forecasting*, **6**, 538–547.

Dyer, A. J. and B. B. Hicks, 1970: Flux-gradient relationships in the constant flux layer. *Quart. J. Roy. Meteor. Soc.*, **96**, 715–721.

Eliassen, A., 1951: Slow thermally or frictionally controlled meridional circulation in a circular vortex. *Astrophys. Norv.*, **5**, 19–60.

Hakim, G. J., 2000: Climatology of coherent structures on the extratropical tropopause. *Mon. Wea. Rev.*, **128**, 385–406.

Hakim, G. J. and A. K. Canavan, 2005: Observed cyclone-anticyclone tropopause asymmetries. *J. Atmos. Sci.*, **62 (1)**, 231–240.

Hakim, G. J., D. Keyser, and L. F. Bosart, 1995: The Ohio Valley wave-merger cyclogenesis event of 25-26 january 1978. Part I: Multiscale case study. *Mon. Wea. Rev.*, **123**, 2663–2692.

Hakim, G. J., D. Keyser, and L. F. Bosart, 1996: The Ohio Valley wave-merger cyclogenesis event of 25-26 january 1978. Part II: Diagnosis using quasigeostrophic potential vorticity inversion. *Mon. Wea. Rev.*, **124**, 2176–2205.

Holton, J. R., 1992: *An introduction to dynamic meteorology*. Academic Press, 511 pp.

Hong, S. .-Y., J. Dudhia, and S. .-H. Chen, 2004: A revised approach to ice microphysical processes for the bulk parameterization of clouds and precipitation. *Mon. Wea. Rev.*, **132**, 103–120.

Hong, S. .-Y. and H. .-L. Pan, 1996: Nonlocal boundary layer vertical diffusion in a medium-range forecast model. *Mon. Wea. Rev.*, **124 (10)**, 2322–2239.

Intrieri, J. M., C. W. Fairall, M. D. Shupe, P. O. G. Persson, E. L. Andreas, P. S. Guest, and R. E. Moritz, 2002: An annual cycle of Arctic surface cloud forcing at SHEBA. *J. Geophys. Res.*, **107 (8039)**, doi:10.1029/2000JC000423.

IPCC, 2007: *The physical basis. Contribution of Working Group I to the Fourth Assessment*

Report of the Introgovernmental Panel on Climate Change. Cambridge University Press, Cambridge, United Kingdom and New York, NY, USA, 996 pp.

Kain, J. S. and J. M. Fritsch, 1993: Convective parameterization for mesoscale models: The Kain-Fritsch scheme. *The representation of cumulus convection in numerical models*, K. A. Emmanuel and D. J. Raymond, Eds., Amer. Meteor. Soc., 246 pp.

Kalnay, E. and collaborators, 1996: The NCEP/NCAR 40-year reanalysis project. *Bull. Amer. Meteor. Soc.*, **77**, 437–472.

Lackmann, G. M., 2002: Cold-frontal potential vorticity maxima, the low-level jet, and moisture transport in extratropical cyclones. *Mon. Wea. Rev.*, **130**, 59–74.

Manabe, S. and R. F. Strickler, 1964: Thermal equilibrium of the atmosphere with a convective adjustment. *J. Atmos. Sci.*, **21**, 361–385.

Mlawer, E. J., S. J. Taubman, P. D. Brown, M. J. Iacono, and S. A. Clough, 1997: Radiative transfer for inhomogeneous atmosphere: RRTM, a validated correlated-k model for the longwave. *J. Geophys. Res.*, **102 (D14)**, 16 663–16 682.

Morgan, M. C. and J. W. Nielsen-Gammon, 1998: Using tropopause maps to diagnose midlatitude weather systems. *Mon. Wea. Rev.*, **126**, 2555–2579.

Paulson, C. A., 1970: The mathematical representation of wind speed and temperature profiles in the unstable atmospheric surface layer. *J. Appl. Meteor.*, **9**, 857–861.

Pedlosky, J., 1998: *Geophysical Fluid Dynamics*, Vol. 84. 2d ed., Springer, 728 pp.

Peixoto, J. P. and A. H. Oort, 1992: *Physics of climate*. 2d ed., American Institute of Physics.

Serreze, M. C., A. P. Barrett, A. G. Slater, M. Steele, J. Zhang, and K. E. Trenberth, 2007: The large-scale energy budget of the Arctic. *J. Geophys. Res.*, **112 (D11122)**, doi:10.1029/2006JD008230.

Skamarock, W. C., J. B. Klemp, J. Dudhia, D. O. Gill, D. M. Barker, W. Wang, and J. G. Powers, 2005: A description of the advanced research WRF version 2. Tech. rep., NCAR.

Stoelinga, M. T., 1996: A potential vorticity-based study of the role of diabatic heating and friction in a numerically simulated baroclinic cyclone. *Mon. Wea. Rev.*, **124 (5)**, 849–874.

Uccellini, L. W., D. Keyser, K. F. Brill, and C. H. Wash, 1985: The President's Day cyclone of 18-19 february 1979: Influence of upstream trough amplification and assoicated tropopause folding on rapid cyclogenesis. *Mon. Wea. Rev.*, **113**, 962–988.

Walsh, J. E., W. L. Chapman, and D. H. Portis, 2009: Arctic cloud fraction and radiative fluxes in atmospheric reanalyses. *J. Climate*, **22 (9)**, 2316–2334.

Webb, E. K., 1970: Profile relationships: The log-linear range, and extension to strong stability. *Quart. J. Roy. Meteor. Soc.*, **96**, 67–90.

Zierl, B. and V. Wirth, 1997: The influence of radiation on tropopause behaviour and stratosphere-troposphere exchange in an upper tropospheric anticyclone. *J. Geophys. Res.*, **102 (23)**, 883–894.

List of Figures

1 Area-weighted occurrence of tropopause polar cyclone intensification during the period 1948-1999 (contours) with the model domain boundary (black box). Values are equal to the number of unique vortices within a 5° latitude × 15° longitude box divided by the cosine of latitude (contour interval of 50). Dashed lines correspond to the 50, 100 and 150 contours while solid lines correspond to the 200, 250, and 300 contours. Only vortices lasting at least two days and that spent at least 60% of their lifetimes north of 65°N latitude are included. Locations of radiosonde stations are denoted by the '+' symbols. 33

2 Tropopause polar cyclonic vortex structural properties of the maximum (a) amplitude and (b) radius from 2 August, 2007 to 31 July, 2009. The filtered cyclone distribution discussed in the text is given by solid lines, and the total vortex distribution is given by the dashed line. 34

3 WRF model tropopause potential temperature model bias for the (a) 24-hour and (b) 48-hour forecast. Locations of radiosonde stations within the domain are denoted by the '+' symbols. The solid black contour denotes the location of the background cross section. 35

4 West–east cross-vortex 24-hour WRF forecast model bias of (a) potential temperature (contour interval 0.5 K), (b) water vapor mixing ratio (contour interval 0.02 g/kg), (c) 500 hPa geopotential height (contour interval 1 meter), and (d) tropopause potential temperature (contour interval 0.25 K). In (a) and (b), the solid black line is the WRF composite tropopause while the dashed gray line is the GFS composite tropopause with a contour interval of 30 meters. In (c) and (d), the heavy solid contours correspond to the WRF composite field while the heavy dashed contours correspond to the GFS composite field, with a contour interval of 5 K. The zero contour is denoted by the thin, solid contour. 36

5 Tropopause polar cyclone sample density from 2 August 2007 to 31 July 2009. Values are equal to the number of unique vortices within a 5° latitude × 15° longitude box divided by the cosine of latitude. 37

6 (a) SKEWT-log p diagram of composite temperature and dewpoint temperature at the vortex core (solid) and at the background grid point (dashed). (b) Vortex core difference plots of temperature (solid) and relative humidity (dashed). The plots to the right of each panel show the corresponding PV in (a) and PV anomaly from the background in (b), in units of PVU, at the vortex core (solid) and background grid point (dashed). Plots are valid at the model analysis time. 38

7 SKEWT–log-p diagram of composite temperature and dewpoint temperature at the vortex core (solid) and at the background grid point (dashed) for (a) winter (December, January, February), (b) spring (March, April, May), (c) summer (June, July, August), and (d) autumn (September, October, November). The plots to the right of each panel show the corresponding PV, in units of PVU, at the vortex core (solid) and background grid point (dashed). Plots are valid at the model analysis time. 39

8 Composite (a) tropopause potential temperature (contour interval is 2 K) and (b) 500 hPa geopotential height (contour interval 30 meters) centered on the vortex core. 40

9 Composite west–east cross-vortex sections of the anomalous (a) temperature (K), (b) v-wind component ($\mathrm{m\,s^{-1}}$), (c) Ertel Potential Vorticity (PVU), and (d) relative humidity (%). The thick, solid black contour is the composite tropopause for the vortex sample, while the thick, dashed black contour is the composite tropopause for a fixed (background) cross section. The zero contour is denoted by the thin, solid contour. 41

10 Composite west–east cross-vortex sections of the (a) total diabatic heating rate, (b) total diabatic heating rate anomalies, (c) radiative heating rate, (d) radiative heating rate anomalies, (e) latent heating rate, and (f) latent heating rate anomalies. Units are in K day^{-1} and the contour interval is 0.3 K day^{-1} in (a),(c),(e) and 0.2 K day^{-1} in (b),(d),(f). The thick, solid black contour is the composite tropopause for the vortex sample, while the thick, dashed black contour is the composite tropopause for a fixed cross section. The zero contour is denoted by the thin, solid contour. 42

11 Composite west–east cross-vortex sections of the (a) vertical motion (Pa s^{-1}) with the (b) symmetric and (c) asymmetric components, and (d) geostrophic vorticity (colors, s^{-1}) and geostrophic vorticity advection by the thermal wind (contours, s^{-2}). Solid (dashed) contours in (b) correspond to values of positive (negative) geostrophic vorticity advection. The color interval is 0.01 Pa s^{-1} in (a), 0.2×10^{-4} s^{-1} in (b), and the contour interval is 0.4×10^{-13} s^{-2} in (d). The thick, solid black contour is the composite tropopause for the vortex sample, while the thick, dashed black contour is the composite tropopause for a fixed cross section. The zero contour is denoted by the thin, solid contour. 43

12 Composite west–east cross-vortex sections of the anomalous EPV tendency due to (a) all diabatic effects, (b) radiation, (c) latent heating, and (d) all diabatic effects except for radiation and latent heating. Units are in PVU day^{-1} and the contour interval is 0.04 PVU day^{-1}. The thick, solid black contour is the composite tropopause for the vortex sample, while the thick, dashed black contour is the composite tropopause for a fixed cross section. The zero contour is denoted by the thin, solid contour. 44

13 Composite tropopause potential temperature anomalies (K) in the (a) winter (DJF), (b) spring (MAM), (c) summer (JJA), and (d) autumn (SON) with a contour interval of 2 K. The zero contour is denoted by the bold, solid contour. The total number of samples used in the vortex composite is 132 for DJF, 159 for MAM, 146 for JJA, and 131 for SON. 45

14 Composite west–east cross-vortex sections of the anomalous (a)-(b) temperature (K), (c)-(d) relative humidity (%), and (e)-(f) radiative heating rate (K day^{-1}) in the winter (DJF, left column) and summer (JJA, right column). The contour interval is 1 K in (a), 3% in (b), and 0.2 K day^{-1} in (c). The thick, solid black contour is the composite tropopause for the vortex sample, while the thick, dashed black contour is the composite tropopause for a fixed cross section. The total number of samples used in the vortex composite for DJF is 132 and 146 for JJA. The zero contour is denoted by the thin, solid contour. 46

15 Composite west–east cross-vortex sections of the anomalous EPV tendency due to (a)-(b) all diabatic effects, (c)-(d) radiation, and (e)-(f) latent heating in the winter (DJF, left column) and summer (JJA, right column). Units are in PVU day^{-1} and the contour interval is 0.04 PVU day^{-1}. The thick, solid black contour is the composite tropopause for the vortex sample, while the thick, dashed black contour is the composite tropopause for a fixed cross section. The total number of samples used in the vortex composite for DJF is 132 and 146 for JJA. The zero contour is denoted by the thin, solid contour. 47

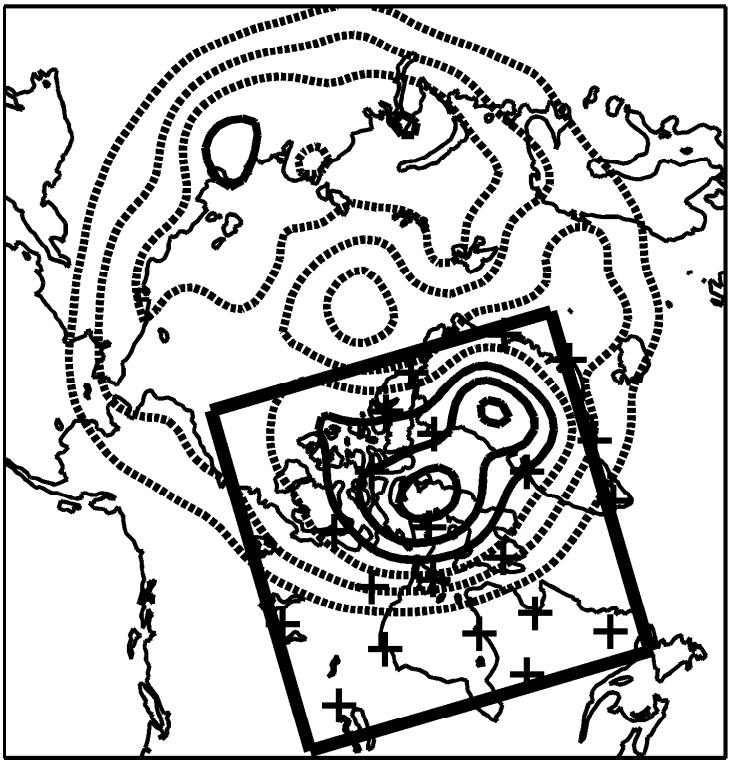

FIG. 1. Area-weighted occurrence of tropopause polar cyclone intensification during the period 1948-1999 (contours) with the model domain boundary (black box). Values are equal to the number of unique vortices within a 5° latitude × 15° longitude box divided by the cosine of latitude (contour interval of 50). Dashed lines correspond to the 50, 100 and 150 contours while solid lines correspond to the 200, 250, and 300 contours. Only vortices lasting at least two days and that spent at least 60% of their lifetimes north of 65°N latitude are included. Locations of radiosonde stations are denoted by the '+' symbols.

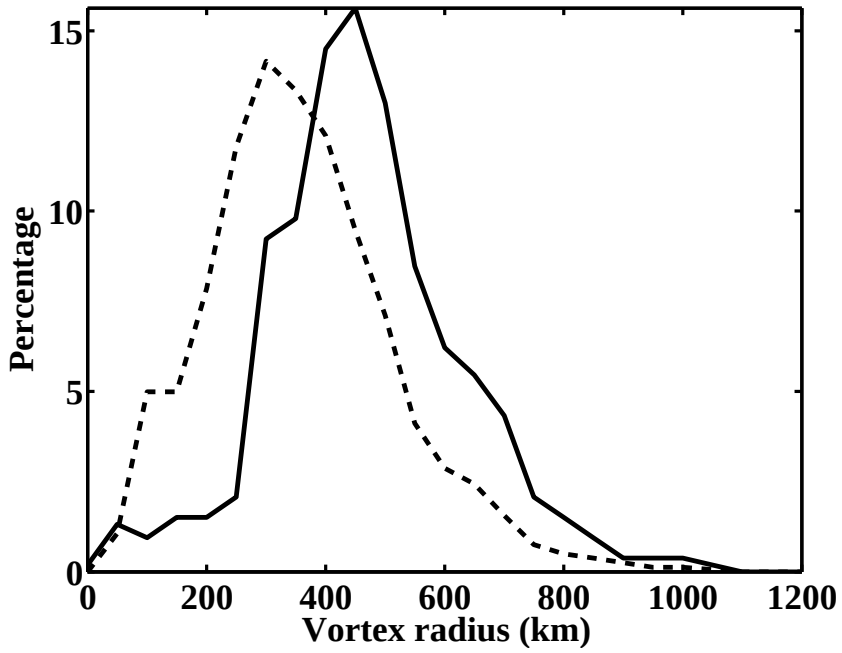

(a)

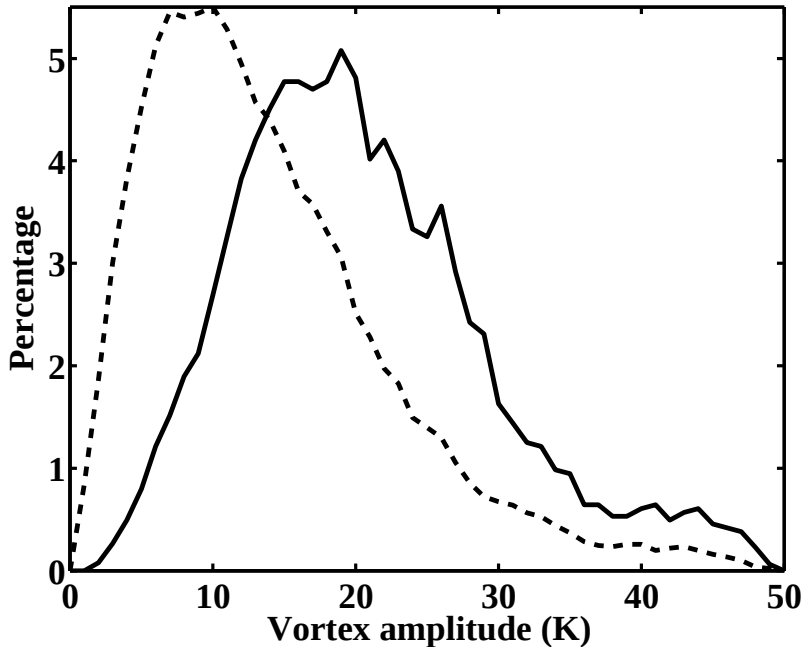

(b)

FIG. 2. Tropopause polar cyclonic vortex structural properties of the maximum (a) amplitude and (b) radius from 2 August, 2007 to 31 July, 2009. The filtered cyclone distribution discussed in the text is given by solid lines, and the total vortex distribution is given by the dashed line.

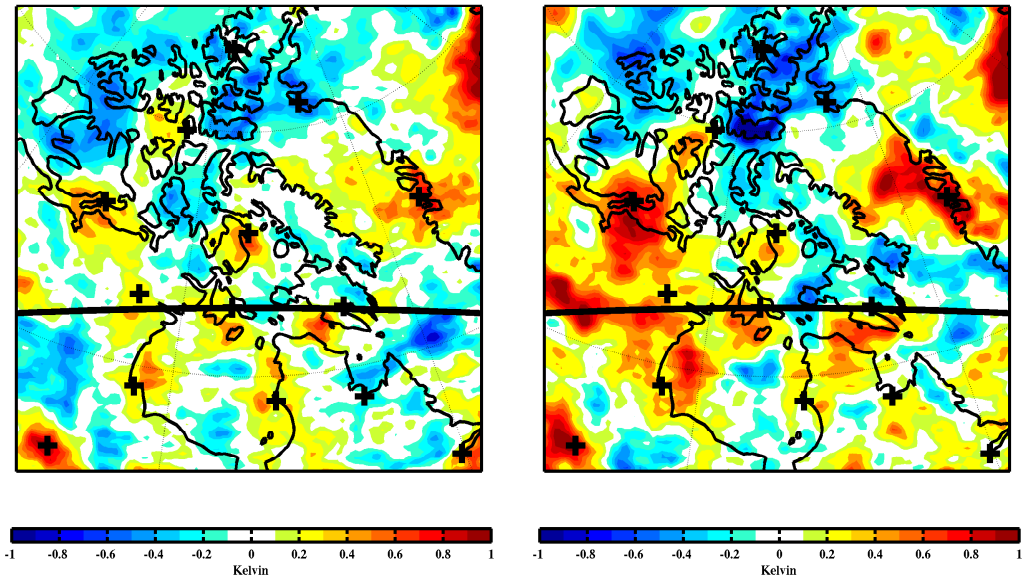

(a) (b)

FIG. 3. WRF model tropopause potential temperature model bias for the (a) 24-hour and (b) 48-hour forecast. Locations of radiosonde stations within the domain are denoted by the '+' symbols. The solid black contour denotes the location of the background cross section.

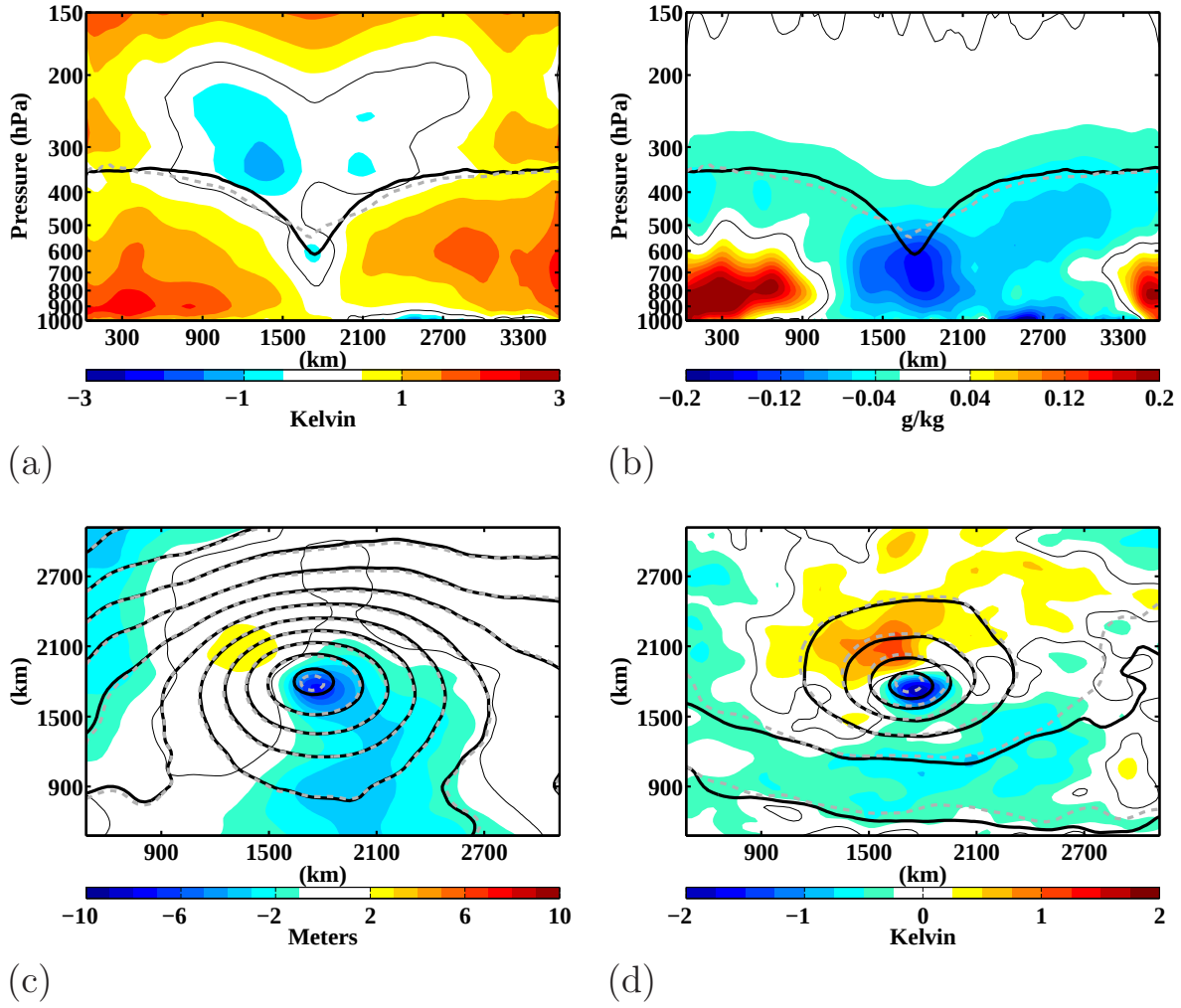

FIG. 4. West–east cross-vortex 24-hour WRF forecast model bias of (a) potential temperature (contour interval 0.5 K), (b) water vapor mixing ratio (contour interval 0.02 g/kg), (c) 500 hPa geopotential height (contour interval 1 meter), and (d) tropopause potential temperature (contour interval 0.25 K). In (a) and (b), the solid black line is the WRF composite tropopause while the dashed gray line is the GFS composite tropopause with a contour interval of 30 meters. In (c) and (d), the heavy solid contours correspond to the WRF composite field while the heavy dashed contours correspond to the GFS composite field, with a contour interval of 5 K. The zero contour is denoted by the thin, solid contour.

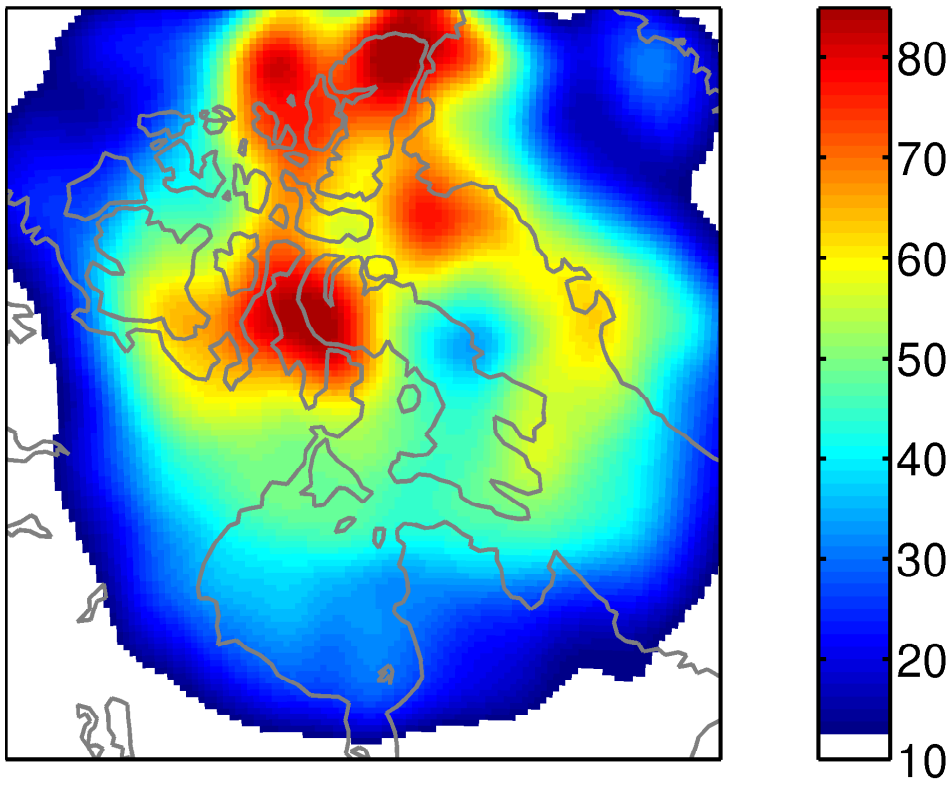

FIG. 5. Tropopause polar cyclone sample density from 2 August 2007 to 31 July 2009. Values are equal to the number of unique vortices within a 5° latitude × 15° longitude box divided by the cosine of latitude.

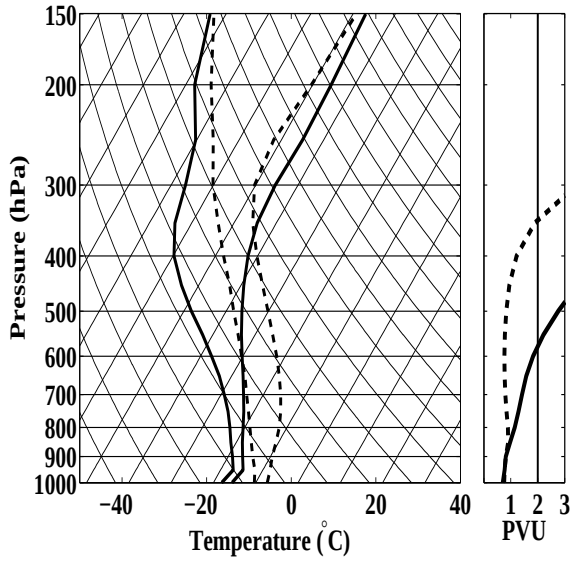

(a)

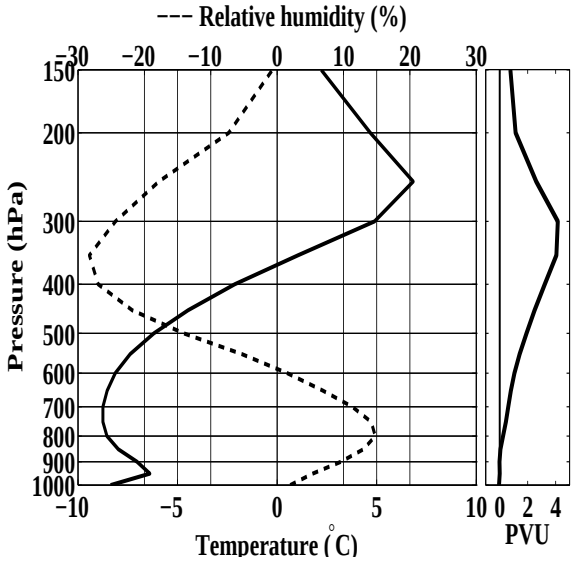

(b)

FIG. 6. (a) SKEWT-log p diagram of composite temperature and dewpoint temperature at the vortex core (solid) and at the background grid point (dashed). (b) Vortex core difference plots of temperature (solid) and relative humidity (dashed). The plots to the right of each panel show the corresponding PV in (a) and PV anomaly from the background in (b), in units of PVU, at the vortex core (solid) and background grid point (dashed). Plots are valid at the model analysis time.

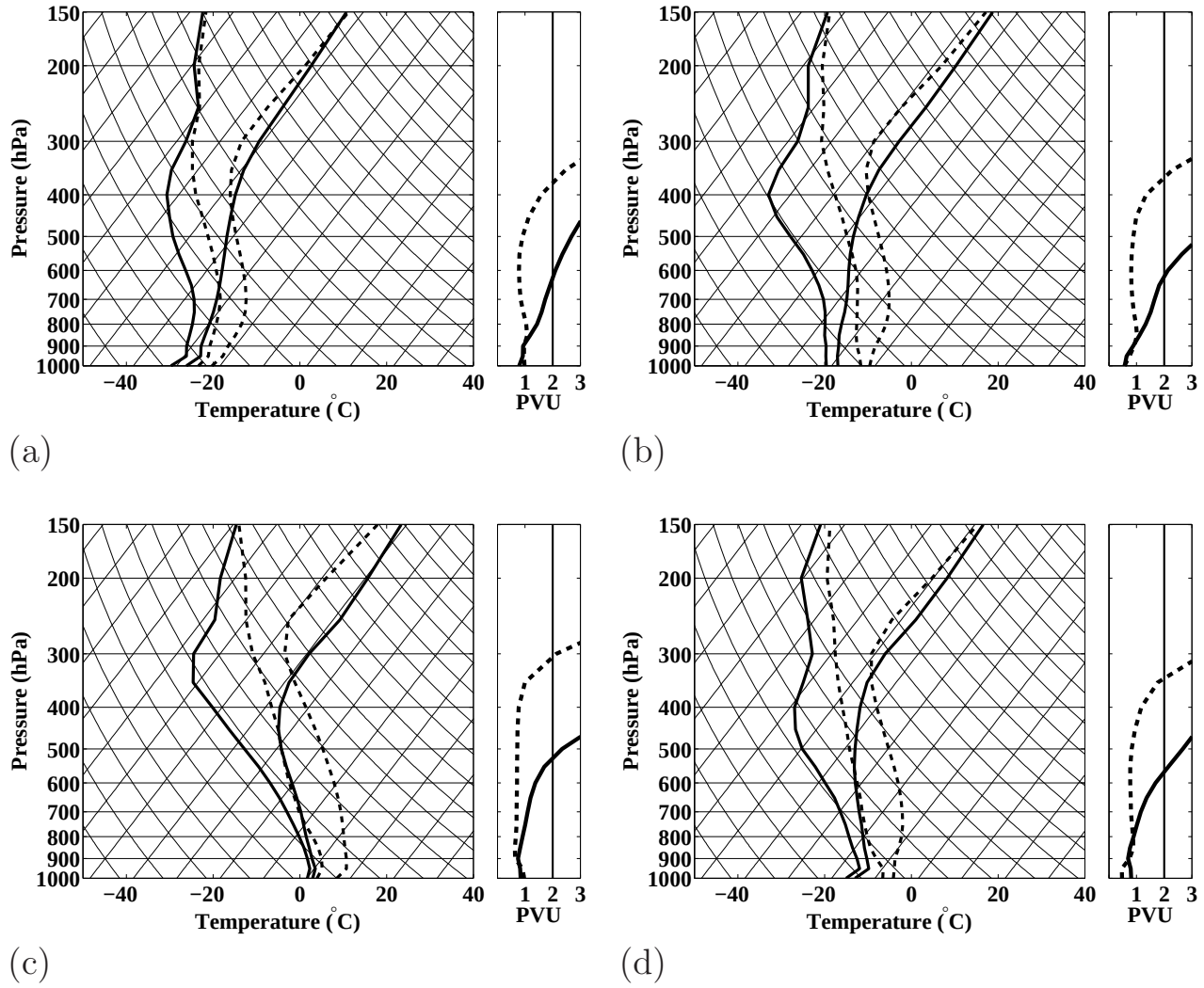

FIG. 7. SKEWT–log-p diagram of composite temperature and dewpoint temperature at the vortex core (solid) and at the background grid point (dashed) for (a) winter (December, January, February), (b) spring (March, April, May), (c) summer (June, July, August), and (d) autumn (September, October, November). The plots to the right of each panel show the corresponding PV, in units of PVU, at the vortex core (solid) and background grid point (dashed). Plots are valid at the model analysis time.

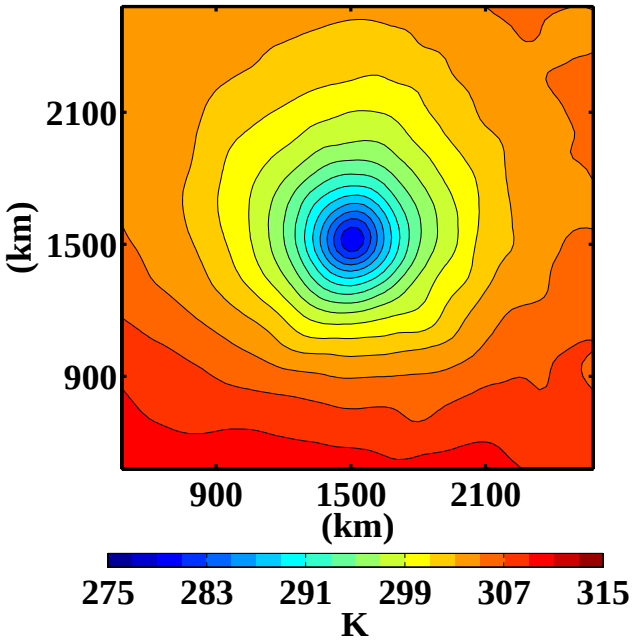

(a)

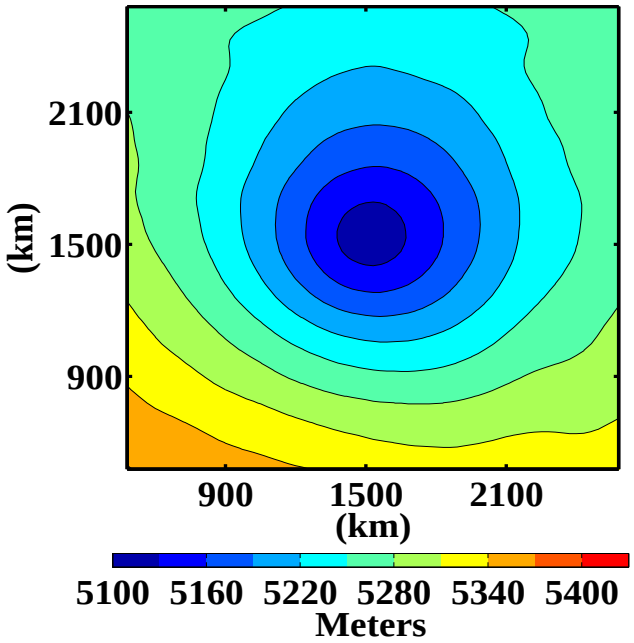

(b)

FIG. 8. Composite (a) tropopause potential temperature (contour interval is 2 K) and (b) 500 hPa geopotential height (contour interval 30 meters) centered on the vortex core.

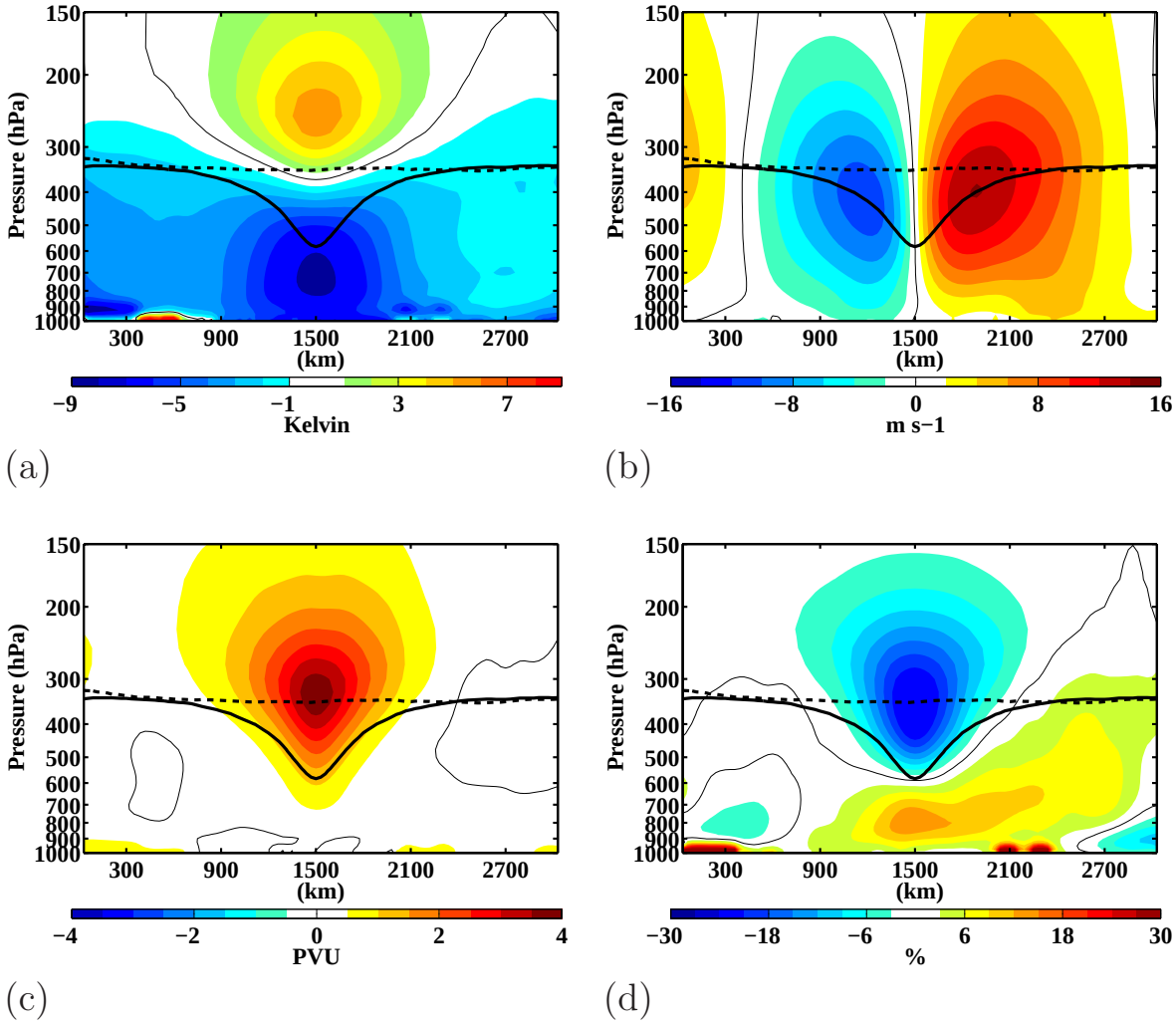

FIG. 9. Composite west–east cross-vortex sections of the anomalous (a) temperature (K), (b) v-wind component ($\mathrm{m\,s^{-1}}$), (c) Ertel Potential Vorticity (PVU), and (d) relative humidity (%). The thick, solid black contour is the composite tropopause for the vortex sample, while the thick, dashed black contour is the composite tropopause for a fixed (background) cross section. The zero contour is denoted by the thin, solid contour.

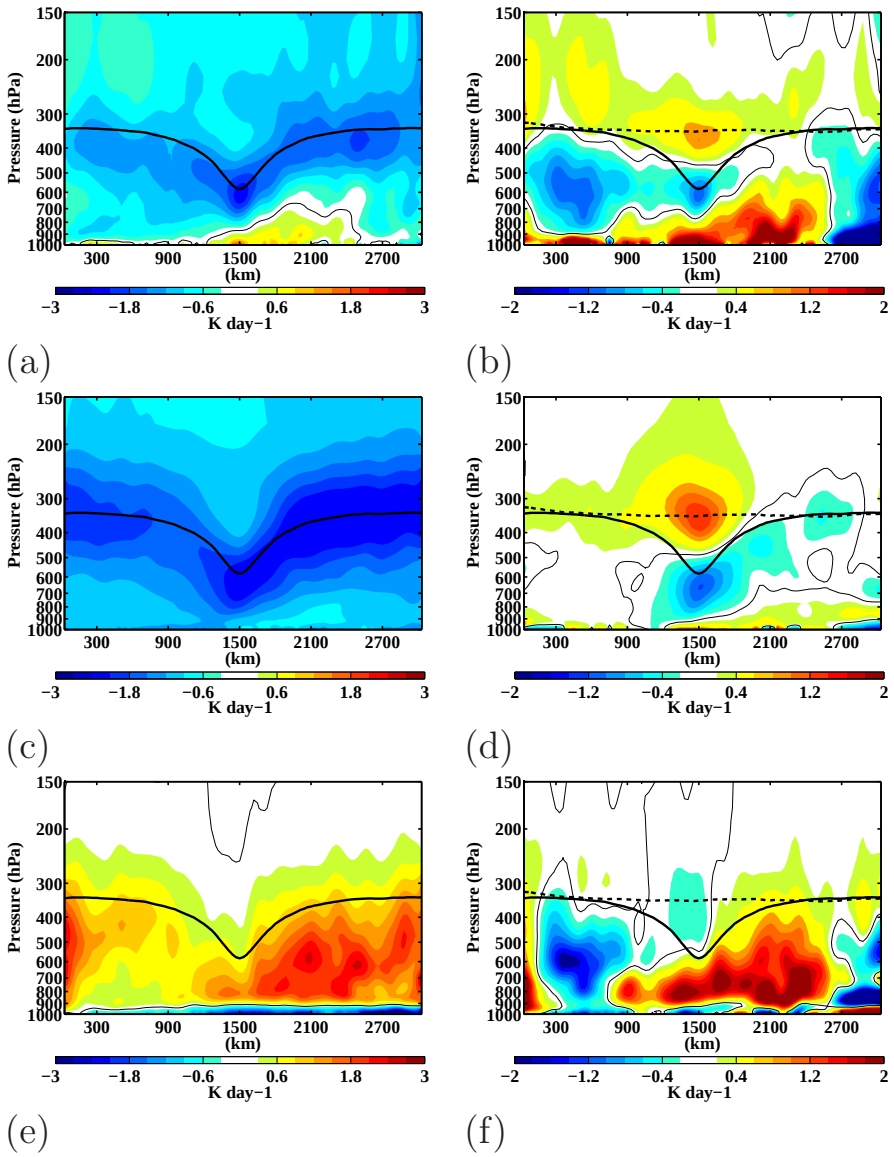

FIG. 10. Composite west–east cross-vortex sections of the (a) total diabatic heating rate, (b) total diabatic heating rate anomalies, (c) radiative heating rate, (d) radiative heating rate anomalies, (e) latent heating rate, and (f) latent heating rate anomalies. Units are in K day^{-1} and the contour interval is 0.3 K day^{-1} in (a),(c),(e) and 0.2 K day^{-1} in (b),(d),(f). The thick, solid black contour is the composite tropopause for the vortex sample, while the thick, dashed black contour is the composite tropopause for a fixed cross section. The zero contour is denoted by the thin, solid contour.

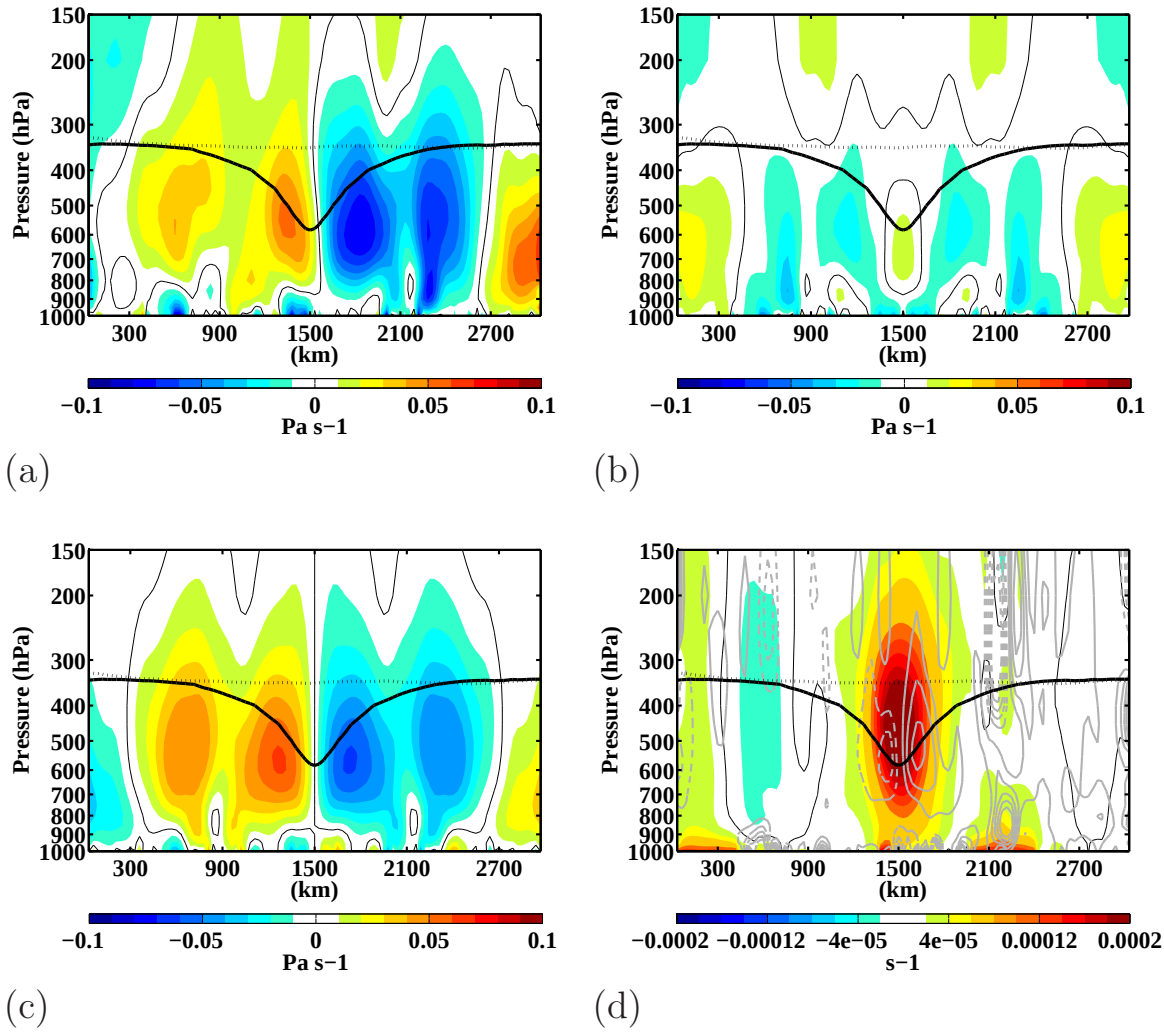

FIG. 11. Composite west–east cross-vortex sections of the (a) vertical motion (Pa s^{-1}) with the (b) symmetric and (c) asymmetric components, and (d) geostrophic vorticity (colors, s^{-1}) and geostrophic vorticity advection by the thermal wind (contours, s^{-2}). Solid (dashed) contours in (b) correspond to values of positive (negative) geostrophic vorticity advection. The color interval is 0.01 Pa s^{-1} in (a), 0.2×10^{-4} s^{-1} in (b), and the contour interval is 0.4×10^{-13} s^{-2} in (d). The thick, solid black contour is the composite tropopause for the vortex sample, while the thick, dashed black contour is the composite tropopause for a fixed cross section. The zero contour is denoted by the thin, solid contour.

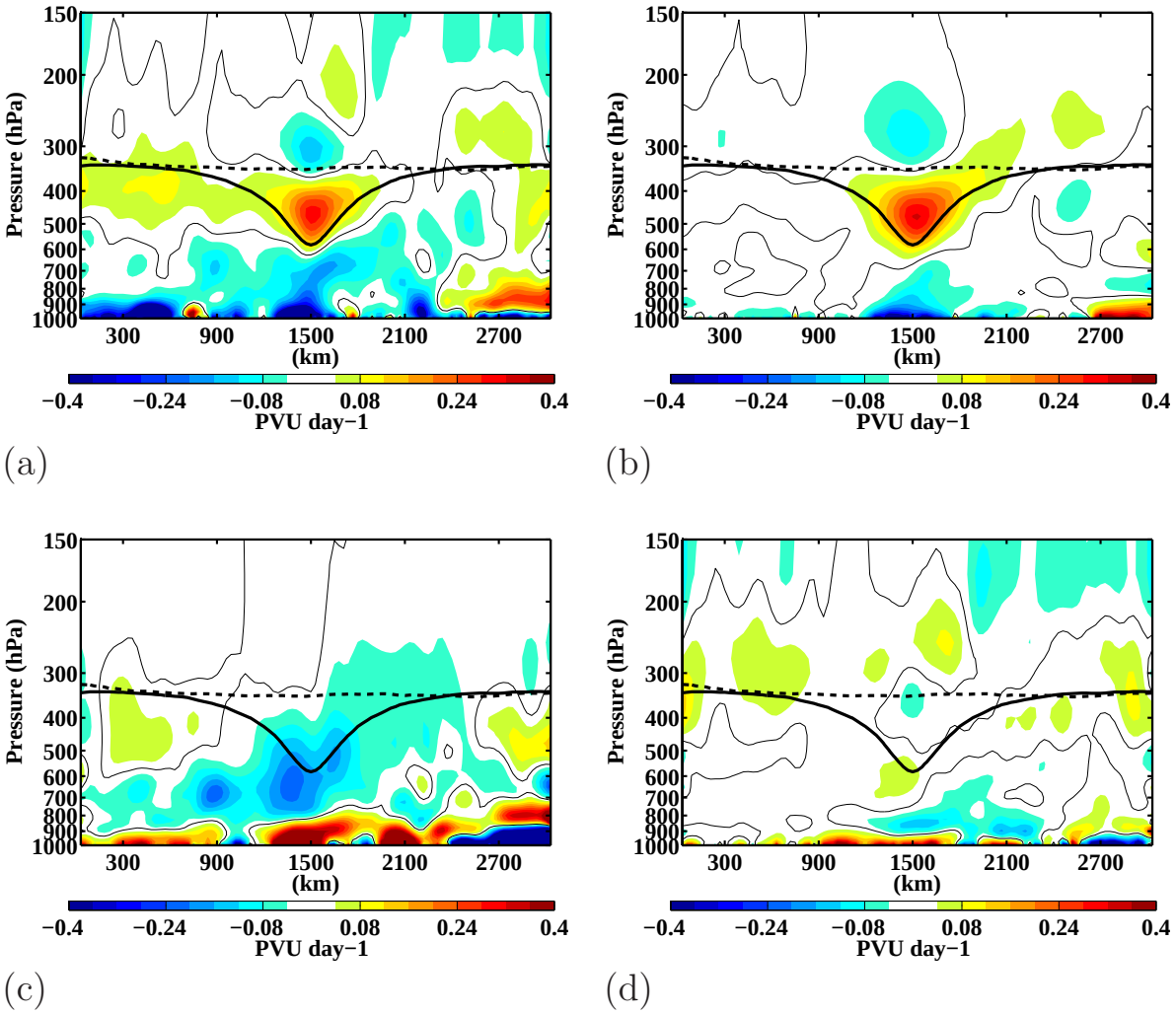

FIG. 12. Composite west–east cross-vortex sections of the anomalous EPV tendency due to (a) all diabatic effects, (b) radiation, (c) latent heating, and (d) all diabatic effects except for radiation and latent heating. Units are in PVU day^{-1} and the contour interval is 0.04 PVU day^{-1}. The thick, solid black contour is the composite tropopause for the vortex sample, while the thick, dashed black contour is the composite tropopause for a fixed cross section. The zero contour is denoted by the thin, solid contour.

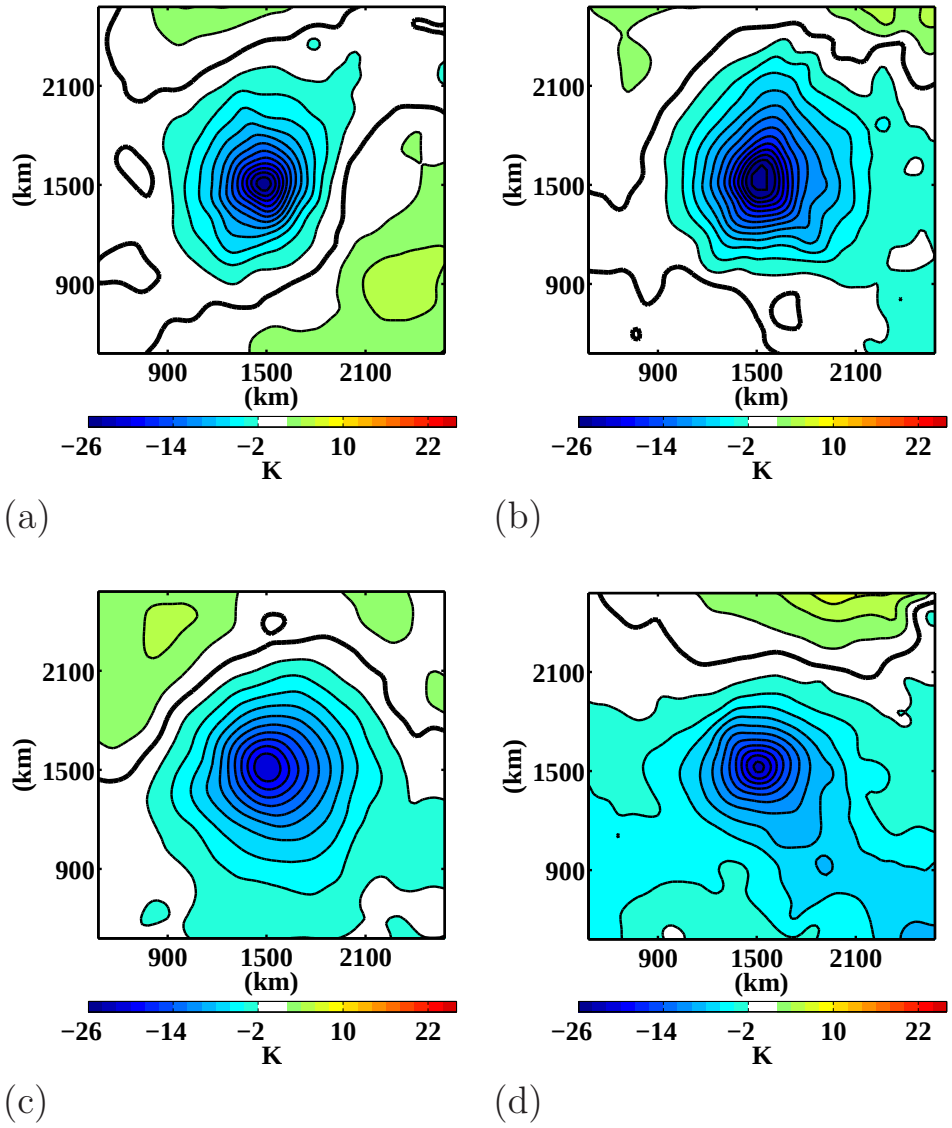

FIG. 13. Composite tropopause potential temperature anomalies (K) in the (a) winter (DJF), (b) spring (MAM), (c) summer (JJA), and (d) autumn (SON) with a contour interval of 2 K. The zero contour is denoted by the bold, solid contour. The total number of samples used in the vortex composite is 132 for DJF, 159 for MAM, 146 for JJA, and 131 for SON.

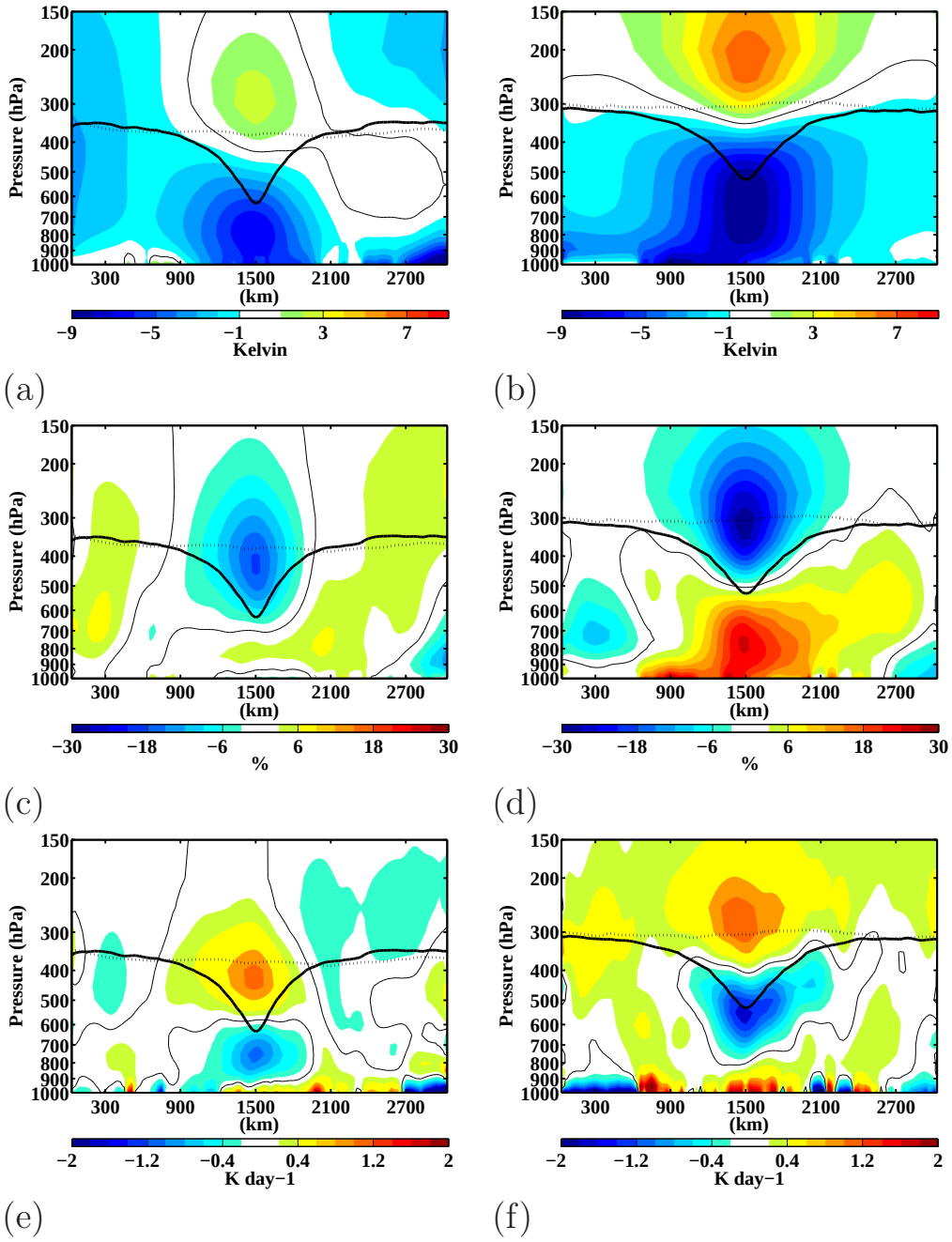

FIG. 14. Composite west–east cross-vortex sections of the anomalous (a)-(b) temperature (K), (c)-(d) relative humidity (%), and (e)-(f) radiative heating rate (K day^{-1}) in the winter (DJF, left column) and summer (JJA, right column). The contour interval is 1 K in (a), 3% in (b), and 0.2 K day^{-1} in (c). The thick, solid black contour is the composite tropopause for the vortex sample, while the thick, dashed black contour is the composite tropopause for a fixed cross section. The total number of samples used in the vortex composite for DJF is 132 and 146 for JJA. The zero contour is denoted by the thin, solid contour.

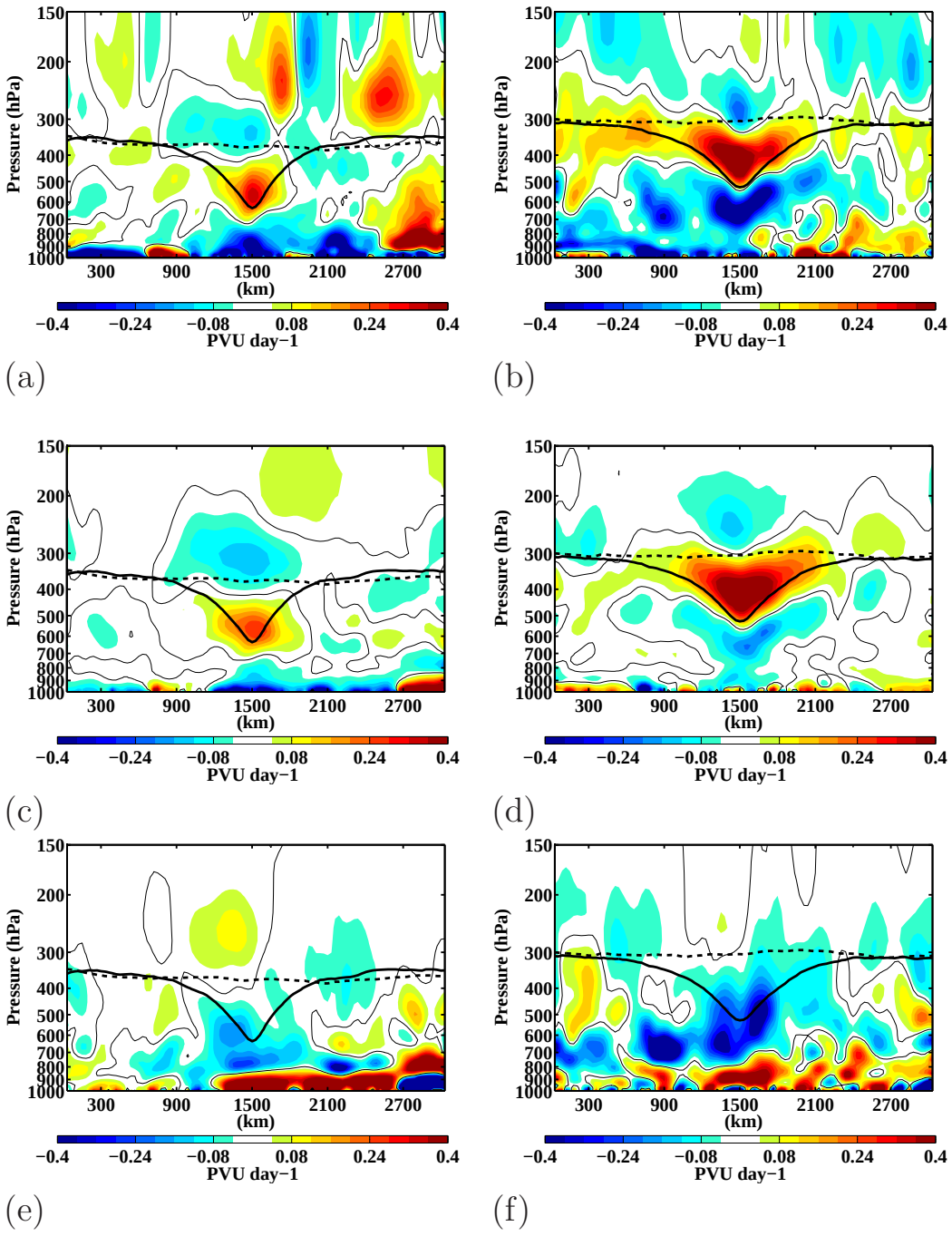

FIG. 15. Composite west–east cross-vortex sections of the anomalous EPV tendency due to (a)-(b) all diabatic effects, (c)-(d) radiation, and (e)-(f) latent heating in the winter (DJF, left column) and summer (JJA, right column). Units are in PVU day^{-1} and the contour interval is 0.04 PVU day^{-1}. The thick, solid black contour is the composite tropopause for the vortex sample, while the thick, dashed black contour is the composite tropopause for a fixed cross section. The total number of samples used in the vortex composite for DJF is 132 and 146 for JJA. The zero contour is denoted by the thin, solid contour.